ORIGINAL ARTICLE

lajss.org© Latin American Journal of Solids and Structures

www.lajss.org

Region-Specific Hard-Impact Response Characteristics of an Airdrop Equipment Subframe Based on Equivalent Drop Tests

Y. Shi[a], S. Yuan[b*], P. Wu[c], B. Hu[b], L. Fu[b], J. X. Luo[a], Z. W. Yang[d]

[a] Key Laboratory of Advanced Manufacturing Technology of the Ministry of Education, Guizhou University, Guiyang, 550025, China. E-mails: gs.shiy24@gzu.edu.cn, 3037521892@qq.com
[b] School of Mechanical Engineering, Guizhou Institute of Technology, Guiyang, 550025, China. E-mails: syuan@git.edu.cn, 1335103838@qq.com, flei6634@163.com
[c] State Key Laboratory of Public Big Data, Guizhou University, Guiyang, 550025, China. E-mail: pengwu@gzu.edu.cn
[d] Guizhou Aerospace Tianma Electromechanical Technology Co., Ltd., Zunyi, 563000, China. E-mail: yangzhengwen86@163.com

*Corresponding author

https://doi.org/10.1590/1679-7825/e9221

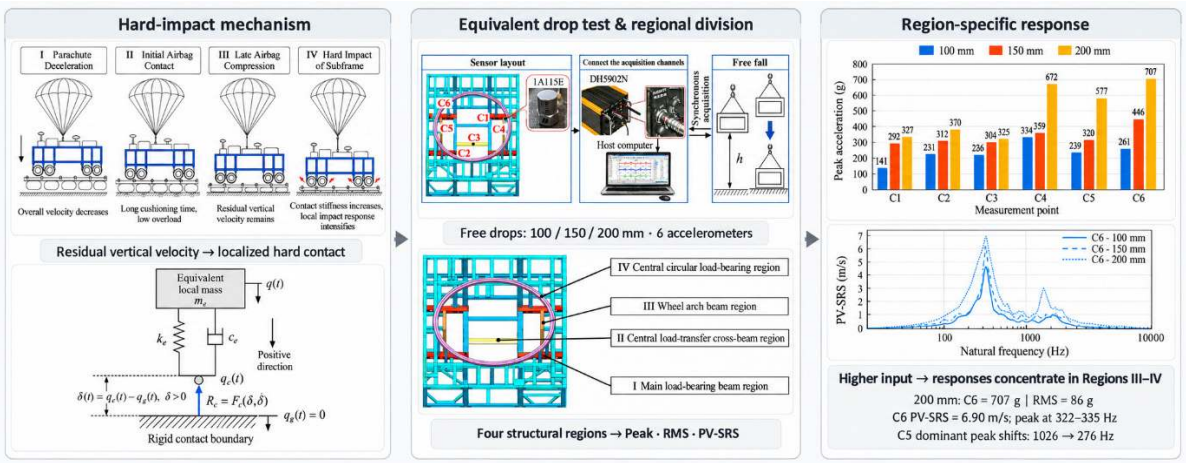
Abstract

Residual vertical velocity during late-stage airbag cushioning can cause localized hard contact between an airdrop-equipment subframe and the ground, which whole-vehicle overload measurements cannot resolve. This study characterizes region-specific hard-impact responses and identifies vulnerable subframe regions. An equivalent contact framework based on residual-velocity equivalence considered contact reaction force, load-transfer paths, and regional dynamic responses. Free-drop tests (100, 150, 200 mm) used a four-region subframe and six uniaxial accelerometers at 50 kHz. Records (0.4 s) were wavelet-detrended and 10 kHz low-pass filtered. Peak acceleration, RMS acceleration, and pseudo-velocity shock response spectrum (PV-SRS) were evaluated. Responses concentrated in the wheel-arch beam and central circular load-bearing regions. At 200 mm, C6 had peak acceleration 707 g, RMS 86 g, and PV-SRS peak 6.9 m/s, with peak frequency 322–335 Hz; C5's dominant peak shifted from 1 kHz to 276 Hz. The framework reveals hard-impact differences obscured by whole-vehicle measurements and supports landing-impact safety and structural reliability assessment of airdrop equipment.

Keywords

airdrop equipment subframe; hard impact; equivalent drop; region-specific response; PV-SRS.

Graphical abstract



Received July 31, 2026. In revised form September 17, 2026. Accepted September 29, 2026. Available online October 02, 2026.
https://doi.org/10.1590/1679-7825/e9221

Latin American Journal of Solids and Structures. ISSN 1679-7825. Copyright © **2026**. This is an Open Access article distributed under the terms of the Creative Commons Attribution License, which permits unrestricted use, distribution, and reproduction in any medium, provided the original work is properly cited.

INTRODUCTION

In applications such as rapid long-range support, equipment delivery to complex terrain, and emergency disaster relief, airdrop operations can overcome the limitations of ground transportation and enable the rapid deployment of personnel, supplies, and heavy equipment. As airdrop equipment develops toward greater weight, integration, and mobility, impact safety during landing has become increasingly important. For an airdrop vehicle, the subframe is the primary structure that carries impact loads and is also critical to the integrity of the entire vehicle. Its structural safety therefore directly affects whether the equipment can land safely. It is consequently necessary to investigate regional response differences and load-transfer characteristics of the subframe under airdrop landing impacts.

Existing studies have mainly focused on the dynamics of the complete airdrop process, airbag cushioning performance, whole-vehicle overload, and landing attitude. Wang et al. (2025) developed a complete-process dynamic model for heavy-cargo airdrop using a reduced multibody system transfer-matrix method, providing a basis for rapid modeling and parameter optimization of complex airdrop systems. Wang and Yang (2023) established models of exit and out-of-cabin motion based on Kane's equations and investigated state continuity, tow ratio, and suspension-line sail effects in multi-item airdrop operations. Zhang et al. (2024) combined a dynamic model, drop testing, and finite-element analysis to predict the landing vibration response of an airdrop vehicle. Lu et al. (2024) developed a nonlinear finite-element model of a new-generation heavy airborne armored vehicle that included combined airbags, tracks, wheels, and suspension, and analyzed the effects of the complex running system on responses at critical locations. Li et al. (2025) divided vehicle landing into an airbag-cushioning stage and a rigid-collision stage and examined the effects of residual velocity and sideslip angle on landing stability. Zhao et al. (2025) analyzed the effects of high-altitude low-pressure environments and airbag inflation and venting parameters on the cushioning performance of heavy airdrop equipment. These studies established a foundation for whole-vehicle landing dynamics, but addressed impact transmission and local responses within different load-bearing regions of the subframe only to a limited extent.

Airbag compression stroke and venting are key factors affecting the cushioning performance of airdrop vehicles. During the late cushioning stage, the equipment may retain a residual vertical velocity and undergo rigid contact, whereas existing research has primarily concentrated on the flexible airbag-cushioning stage. Shen et al. (2025) described an airbag landing system as a coupled dynamic system comprising rigid bodies, flexible fabric, and internal gas, and indicated that fabric tensioning, slackening, wrinkle transitions, airflow, and contact among multiple airbags jointly determine the landing response. Zhou et al. (2022) investigated the configuration, large deformation, and venting process of combined landing airbags and showed that multi-chamber airbags can improve impact-energy distribution through staged load carrying. Cao and Jin (2010) conducted fluid-structure interaction simulations and drop tests on a flexible airdrop container, finding differences in impact stress among locations and demonstrating that drop height affects local dynamic stress. Fu et al. (2021) analyzed the dynamic responses of a vehicle and critical human-body locations during the soft-landing cushioning of a manned armored vehicle. Lu et al. (2023) investigated the staged cushioning action of inner and outer airbags in a combined airbag system for heavy-equipment airdrop. Li et al. (2022) established an interconnected-airbag model for heavy-equipment airdrop and analyzed the effects of the interconnection structure and gas flow on cushioning performance. If the airbags vent too rapidly or provide an insufficient effective stroke, or if the equipment lands at an inclined attitude, the remaining kinetic energy may be transmitted further to the support members and subframe, causing secondary contact between the vehicle and the ground or a rigid travel-limiting structure. Compared with flexible airbag cushioning, hard impact during the late cushioning stage is characterized by high contact stiffness, a rapid rise in load, a short duration, and localized response concentration. High dynamic responses may occur at beam connections, stiffness transitions, and mass-concentration locations. The research focus should therefore extend from whole-vehicle cushioning performance to load transmission and region-specific response within the subframe.

Multibody dynamics and finite-element simulation have become the principal methods used in airdrop landing research. Yang et al. (2022) established a dynamic model of a vehicle-airbag system and analyzed whole-vehicle overload, local roof acceleration, and structural stress under different conditions. Lian et al. (2022) used LS-DYNA to model heavy equipment and airbags and compared landing responses on rigid and soil surfaces. Zhang et al. (2023) investigated a method for estimating dynamic loads in a tracked running system, providing a basis for modeling load input between the running system and the vehicle body. Simulation accuracy, however, is affected by contact stiffness, damping, friction, boundary conditions, and structural details. Shen et al. (2025) noted that asymmetric deformation of multiple airbags, frictional sliding, and contact under changing boundaries remain difficult to describe accurately. Lu et al. (2024) pointed out that, although omitting tracks, wheels, and suspension can improve computational efficiency, it affects response assessment at low-stiffness locations and critical connections. He et al. (2015) developed a hierarchical updating method for the finite-element model of an airbag cushioning system using measured responses, demonstrating that key parameters in an impact model must be identified and updated through tests. Numerical simulation is therefore suitable

for explaining overall trends and conducting parametric analyses, but local peaks, contact timing, secondary pulses, and frequency-band responses still require validation by impact tests on physical structures. Existing studies have generally used simulated airdrop tests, equivalent drop tests, or full-scale drop-impact tests for validation. Zhang et al. (2024) measured acceleration at the vehicle floor and front-passenger seat during a 1 m free-drop test. Hou et al. (2019) tested the shock and vibration of onboard equipment in an armored vehicle using simulated airdrop tests and found that the measured signals contained three stages: suspension-line impact, primary airbag cushioning, and ground rebound. Timmers et al. (2009) conducted full-scale airbag drop tests of the Orion Crew Module at NASA Langley and used measured pressure and acceleration histories to calibrate the venting coefficient and valve-opening delay in an LS-DYNA model. Equivalent and full-scale tests can therefore not only validate a design, but also identify venting, contact, and delay parameters that are difficult to determine in advance from theoretical models.

For impact-response evaluation, a single peak acceleration value reflects only the transient extreme and cannot simultaneously describe vibration persistence and frequency-dependent response. Xu et al. (2022) compared representative nonlinear contact models and showed that contact stiffness, damping, and coefficient of restitution affect collision force and structural vibration response. Yan and Li (2019, 2021) proposed shock-response-spectrum-based methods for describing the transmission and synthesis characteristics of shock signals in different frequency bands. Different acceleration histories may produce identical or similar response spectra; therefore, SRS cannot fully preserve phase and pulse information from the original time history. Hou and Li (2023) investigated damage boundaries on the response spectrum using an elastic single-degree-of-freedom model and showed that structural responses in different frequency ranges may be controlled by absolute acceleration, pseudo-velocity, and relative displacement, respectively. Evaluation of subframe hard impact should therefore not be limited to comparing peak values at measurement points. Peak acceleration, RMS acceleration, and PV-SRS should be used together to characterize local transient extremes, sustained vibration levels, and frequency-dependent response characteristics, respectively.

In summary, systematic analysis methods have been developed for airbag cushioning and whole-vehicle response, but systematic analyses of the underlying mechanisms and experimental validation remain insufficient with respect to: (1) subframe hard impact induced by residual velocity during the late cushioning stage, (2) the synchronous responses of different load-bearing regions, and (3) differences among multiple evaluation indices. To address these issues, an upper laboratory drop condition was estimated from the specified mean landing-impact acceleration limit and an assumed equivalent impact duration, and free-drop tests were conducted at 100, 150, and 200 mm. Six acceleration measurement points were arranged in the main load-bearing cross-beam region, the central load-transfer cross-beam region, the wheel-arch beam region, and the Central circular load-bearing region. The measured signals were then detrended and low-pass filtered, and peak acceleration, Root Mean Square (RMS) acceleration, and the Pseudo-Velocity Shock Response Spectrum (PV-SRS) were combined to reveal response evolution and frequency-band characteristics in each region. The study aims to extend landing-impact evaluation from whole-vehicle overload to critical load-bearing structures and to provide an experimental basis for improving the structural safety and mission reliability of airdrop equipment under complex landing conditions.

1 OVERVIEW OF THE AIRDROP SCENARIO

1.1 System Components and Role of the Subframe

A schematic of the airdrop equipment system configuration is shown in Fig. 1. The upper auxiliary equipment carries mission equipment, communication devices, and other functional modules; its mass and arrangement affect the overall center-of-mass position and landing attitude of the vehicle. The subframe is the principal load-bearing and load-transmitting structure of the vehicle. It connects the upper equipment, tires, and associated support components and transfers landing-impact loads to the various structural regions. The tires provide elastic support and local cushioning during transportation and landing while also participating in load transfer. The cargo platform secures and supports the complete vehicle and distributes the vehicle load uniformly to the lower cushioning system. The airbags are arranged beneath the cargo platform and extend the impact duration through compression deformation and energy dissipation by venting, thereby reducing landing overload and improving the landing stability of the vehicle.

During the landing of airdrop equipment, the subframe simultaneously performs load-bearing, connection, and impact-load transmission functions. It supports the main body of the equipment and the additional mass. After landing-impact loads are introduced through the airbags or local contact points, they are transmitted and distributed to the equipment body through the subframe longitudinal beams, cross-beams, connection nodes, and connecting structures. Because the structural form, local stiffness, mass distribution, and connection constraints differ among subframe locations, the impact load may undergo local concentration, reflection, and dynamic amplification during transmission,

causing different regions to exhibit different impact-response characteristics. In particular, during the late stage of airbag cushioning, when the compression stroke approaches its limit or a residual vertical velocity remains, the subframe may directly participate in localized hard contact and sustain a short-duration, high-amplitude transient impact. The subframe is therefore not only the principal load-bearing component of the airdrop equipment, but also a key structure governing hard-impact load-transfer paths and local dynamic responses. Its response characteristics are directly related to the impact safety of critical equipment components.

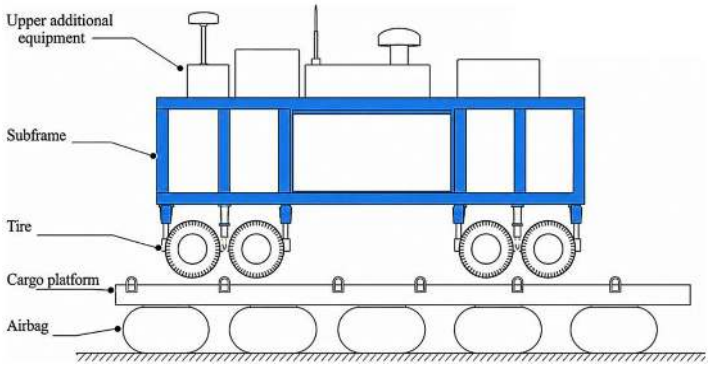


Figure 1 Components of the airdrop vehicle system

1.2 Overview of the Hard-Impact Scenario

From the perspective of landing dynamics, the ground-contact cushioning process of airdrop equipment can be divided into four typical stages, as shown in Fig. 2. Stage I is parachute deceleration, during which the downward velocity of the equipment gradually decreases under the combined effects of gravity, aerodynamic drag, and parachute-system tension. Stage II is initial airbag contact, in which the airbags first contact the ground and begin to deform in compression; impact energy starts to be dissipated through airbag deformation and internal-gas venting. Stage III is the late stage of airbag compression and energy absorption. Airbag deformation approaches the design stroke, venting-based cushioning capacity gradually decreases, and the equipment body may still be moving. Stage IV is hard impact. When airbag cushioning is insufficient, local compression approaches its limit, or the equipment attitude becomes inclined, the subframe and its support structures undergo short-duration, high-stiffness contact with the ground, the end of the cushioning stroke, or another rigid constraint. The present study does not address the complete process from airborne descent to a full stop; instead, it focuses on the hard-impact stage that may occur late in airbag cushioning. During this stage, the load acting on the subframe supports is no longer the comparatively smooth airbag-cushioning load, but a transient impact input governed by the local contact state. In an actual airdrop, residual velocity after venting may cause a hard impact between the equipment and the ground. Analyzing the subframe response during this late-stage hard impact is important for identifying regions of local dynamic amplification, optimizing impact-resistant structural design, and improving the landing reliability of airdrop equipment.

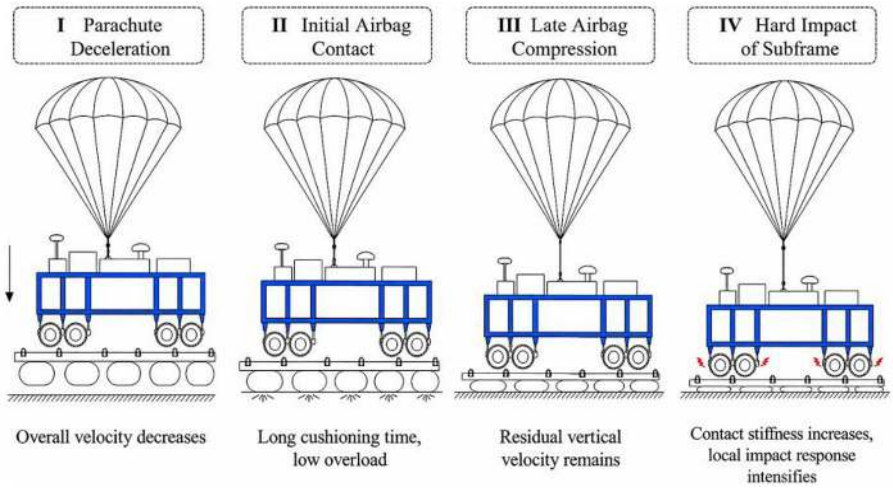


Figure 2 Schematic of the landing-cushioning and hard-impact stages of airdrop equipment

2 EQUIVALENT CONTACT AND REGIONAL RESPONSE MODEL FOR HARD IMPACT

To describe the conversion of residual vertical motion during the late stage of airbag cushioning into a local impact input on the subframe, the initial contact region is represented by the equivalent vertical contact model shown in Fig. 3.

The model establishes the relationship among residual motion, contact reaction force, and the dynamic responses of the structural regions.

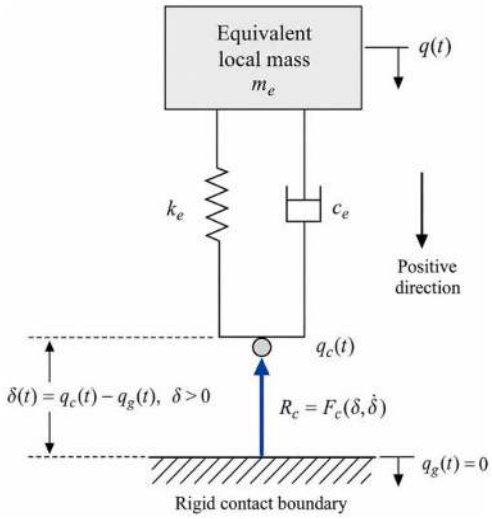


Figure 3 Equivalent model of localized contact during hard impact

Let the vertically downward direction be positive. In the figure, $\boldsymbol{m_e}$ is the equivalent mass involved in the initial contact and impact-load transmission, $\boldsymbol{q(t)}$ is its generalized displacement, $\boldsymbol{q_c(t)}$ is the displacement of the local contact point on the subframe, and $\boldsymbol{q_g(t)}$ is the displacement of the contact boundary. For a free-drop test onto a rigid ground surface, the contact boundary can be regarded as fixed, i.e.,

$$q_g(t) = 0 \tag{1}$$

The connection stiffness and damping between the equivalent mass and the contact point are denoted by k_c and c_c, respectively. Their relative deformation and transmitted force are given by:

$$\Delta_e(t) = q(t) - q_c(t) \tag{2}$$

$$F_e(t) = k_c\Delta_e(t) + c_c\dot{\Delta}_e(t) \tag{3}$$

where $F_e(t)$ is the internal force transmitted from the local support to the upper equivalent mass after contact is established. During hard impact, if the instantaneous effect of gravity and the mass of the contact point are neglected, $F_e(t)$ and the ground reaction force $R_c(t)$ acting on the contact point have equal magnitudes and opposite directions.

The compression between the contact point and the rigid boundary is defined as:

$$\delta(t) = q_c(t) - q_g(t) \tag{4}$$

When $\delta(t) \le 0$, effective compression has not yet developed between the contact point and the rigid boundary, and the contact reaction force is approximately zero. When δ(t) > 0, the local support region enters a compressive-contact state and develops a boundary reaction force. The contact relationship can therefore be written as:

$$R_c(t) = \begin{cases} 0, & \delta(t) \le 0, \\ F_c\left[\delta(t), \dot{\delta}(t)\right], & \delta(t) > 0, \end{cases} \tag{5}$$

where $F_c(\cdot)$ is a contact-force function related to contact stiffness, damping, material restitution characteristics, and contact geometry. Equation (5) indicates that the hard-impact input is jointly determined by the contact compression and compression velocity and is therefore a nonlinear load that varies with the contact state.

After the contact reaction force develops, the impact load propagates to different regions through the bottom supports, wheel-arch beams, longitudinal and transverse beams, and connection nodes. Because the stiffness, mass distribution, connection form, and boundary conditions differ among regions, the propagating load undergoes attenuation, reflection, and superposition along multiple paths. The equivalent dynamic input transmitted to region i can be expressed as

$$p_i(t) = \mathcal{T}_i[R_c(t)] \tag{6}$$

where $\mathcal{T}_i[\cdot]$ is the equivalent transfer operator from the contact point to region i.

To illustrate response differences among regions, region i can be further conceptualized as a local equivalent single-degree-of-freedom system:

$$m_i\ddot{q}_i(t) + c_i\dot{q}_i(t) + k_i q_i(t) = p_i(t) \tag{7}$$

where $q_i(t)$ is the equivalent generalized response of the region, and m_i, c_i, and k_i are the equivalent mass, damping, and stiffness of the region, respectively. Equation (7) is used only to illustrate the influence of regional dynamic parameters and load-transfer paths on the local response; it does not imply that the individual measurement points correspond to mutually independent single-degree-of-freedom systems. The measured acceleration $a_i(t)$ can be regarded as the superposition of the local acceleration and the responses of multiple structural modes.

Equations (5)-(7) show that the region-specific response of the subframe is jointly governed by contact input, load-transfer paths, and regional dynamic parameters. Consequently, under the same hard impact, the Peak acceleration, RMS, and PV-SRS characteristics differ among regions. This provides the theoretical basis for the subsequent regional measurements and multi-index evaluation.

3 STATIC ANALYSIS OF THE SUBFRAME AND EQUIVALENT DROP-TEST PROGRAM

3.1 Development of the Finite-Element Model

The test specimen was the subframe of an airdrop equipment system, whose overall structure is shown in Fig. 4(a). The subframe has a frame composed of longitudinal and transverse beams and mainly comprises longitudinal beams, main load-bearing cross-beams, central load-transfer cross-beams, wheel-arch beams, a Central circular load-bearing structure, and local support members. Its overall envelope dimensions are approximately 3010 mm in length, 2350 mm in width, and 760 mm in height. The primary beams are 6 mm thick and are made of 40Cr steel.

The finite-element model retained the beam system, central annular structure, and connecting members that have major effects on overall stiffness and load transfer, while small holes, chamfers, and other local manufacturing details were neglected. The model was discretized using shell and solid elements. The nominal mesh size in the main region was approximately 10 mm, with local refinement at the central annular structure and the transitions to the wheel-arch beams. The material elastic modulus was 210 GPa, Poisson's ratio was 0.3, and the density was 7800 kg/m^3.

According to the assembly and support relationships of the subframe, constraints were applied at the bottom support locations, and a vertical load was distributed over the central circular load-bearing structure. Three parametric additional-load levels, corresponding to static vertical loads of 3, 6, and 9 t, were considered to provide a graded comparison of the stress magnitude and the spatial distribution of the principal high-stress regions under increasing static loading. The loaded region, load direction, and boundary conditions were kept identical for all three cases. These parametric load levels do not represent the actual mass of the approximately 3.6-t drop-test assembly and are not associated with the three drop-height conditions.

The Von-Mises equivalent-stress distributions under the three conditions are shown in Figs. 4(b)-(d), and the maximum equivalent stresses were 82.94, 126.65, and 163.51 MPa, respectively. As the load increased, the overall structural stress level rose, while high-stress locations remained concentrated mainly at the connections between the central annular structure and the cross-beams, diagonal braces, and support members. Local stress increases also occurred in the transition regions between the wheel-arch beams and the main frame. Stress was relatively low over most of the main longitudinal and transverse beams, indicating that the static load was transmitted primarily from the central annular structure to the surrounding beam system and the bottom supports. This analysis was used to identify

the principal load-transfer paths, local stiffness transitions, and load-concentration locations, thereby providing a basis for subsequent structural region division and measurement-point placement. The static FE results are used only for qualitative identification of load-transfer paths and stress-concentration regions and are not intended to reproduce the transient drop-impact response.

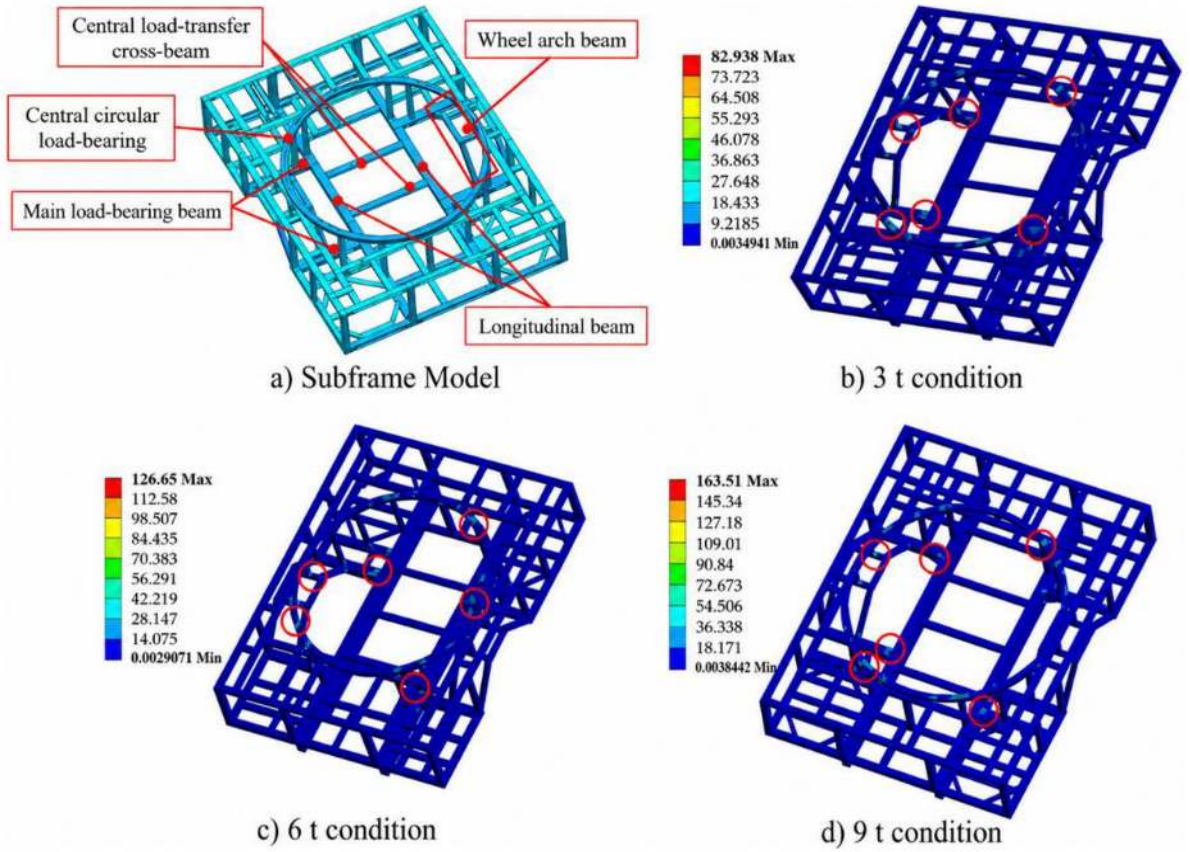


Figure 4 Finite-element model of the subframe and equivalent-stress contours under different static-load conditions

3.2 Region Division Based on Static Characteristics

The static analysis showed that the principal high-stress regions were spatially consistent under the three parametric additional-load conditions. However, static stress magnitude cannot directly represent the local acceleration response during hard impact. Therefore, the regional division was based jointly on structural function, load-transfer characteristics, local configuration, stiffness transitions, and the stress-distribution patterns identified from the static analysis.

Based on these principles, the subframe was divided into four analysis regions, as shown in Fig. 5.

Region I is the main load-bearing cross-beam region. It includes the cross-beams responsible for transmitting the primary load and their connections to the longitudinal beams. Its main function is to distribute local input toward the main frames on both sides. In the static analysis, the overall stress level in this region was lower than that at the central annular connections, although local stress increases occurred at beam-end connections and welded transitions.

Region II is the central load-transfer cross-beam region. Located in the middle of the subframe, it connects the left and right beam systems and transfers loads between regions. Under all three static-load conditions, its stress distribution was relatively continuous, and no localized high-stress region was observed, indicating that its primary function is transitional load transfer.

Region III is the wheel-arch beam region. It includes the wheel-arch beams, side vertical members, and their connections to the main frame. Owing to curvature changes, cross-sectional transitions, and multi-member connections, the local stiffness distribution is comparatively complex.

Region IV is the Central circular load-bearing region. It directly carries the concentrated load from the upper structure and connects to cross-beams, diagonal braces, and support members. It is the principal location at which multiple load-transfer paths converge and are redirected. High stresses occurred in this region and at its connections under all three static-load conditions; it was therefore evaluated as an independent region.

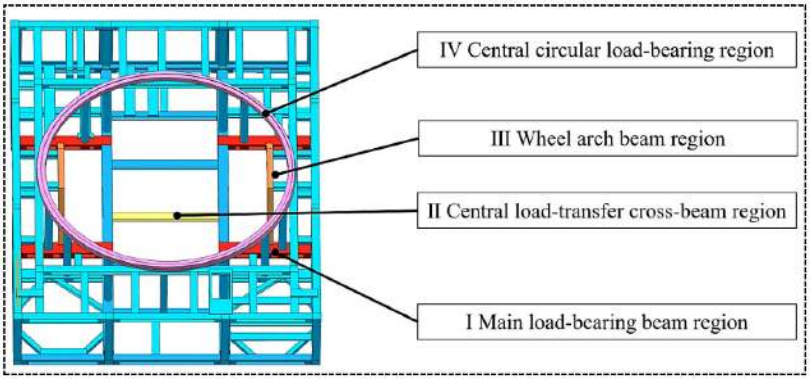


Figure 5 Schematic of the subframe regions

The above division does not treat the subframe as a set of mutually independent structural units. Instead, the analysis regions were defined according to the dominant load-bearing functions of different locations. The static results were used to identify load paths, stiffness transitions, and load-concentration locations, while the regional division additionally considered structural function and local geometric characteristics. This regional division provides a structural basis for the subsequent measurement-point layout and comparisons of Peak acceleration, RMS, and PV-SRS.

3.3 Design of the Equivalent Drop-Impact Test

As discussed above for the hard-impact scenario of airdrop equipment, if a residual vertical velocity remains during the late stage of airbag cushioning, local subframe supports may undergo short-duration, high-stiffness contact with the ground or a rigid constraint. The principal input during this stage can be approximated as the impact generated when the subframe, moving with the residual vertical velocity of the equipment, makes brief contact with the ground. Because a complete airdrop test is difficult to reproduce, the dynamic problem was replicated under laboratory conditions using residual-vertical-velocity equivalence and a free drop to generate the vertical impact input. Neglecting aerodynamic drag, the theoretical impact velocity v is

$$v = \sqrt{2gh} \tag{8}$$

where h is the drop height and g = 9.81 m/s^2.

Approximating the mean deceleration magnitude during impact as

$$a = \frac{v}{T} \tag{9}$$

where T is the effective impact duration.

Combining Equations (8) and (9) gives the drop height:

$$h = \frac{(a \cdot T)^2}{2g} \tag{10}$$

where a is the mean impact acceleration during the impact stage.

Hong et al. (2015) and Academy of Armored Force Engineering, PLA (2017) reported an upper mean landing-impact acceleration of 20 g for airdrop equipment. MIL-STD-810H Method 516.8 provides millisecond-scale reference pulse durations for standardized mechanical shock testing, including an approximately 11 ms reference pulse in the relevant shock-testing context (U.S. Department of Defense, 2022). The value *T*=10 ms was therefore adopted as a rounded engineering approximation rather than a measured parameter of the present equipment. To account for uncertainties in the actual lifting and release attitude, contact sequence, and local structural response, three graded drop heights of 100, 150, and 200 mm were specified to cover hard-impact inputs from relatively low to relatively high levels. The theoretical impact velocity and specific energy per unit mass for the three conditions are listed in Table1.

Table 1 Input parameters for the drop-test conditions

Drop height	Impact velocity	Specific energy per unit mass
$h\ (mm)$	$v\ (m \cdot s^{-1})$	$e\ (J \cdot kg^{-1})$
100	1.400	0.98
150	1.715	1.47
200	1.980	1.96

The test specimen was the subframe of a specific type of airdrop equipment. The subframe mass was approximately 1.2 t and the additional mass was approximately 2.4 t; the primary subframe material was 40Cr steel. During the test, the subframe was lifted by a crane to the specified height and released, and the impact-acceleration responses at all measurement points were acquired after ground contact.

3.4 Sensor Layout and Test Procedure

To obtain local acceleration responses in different structural regions of the subframe during hard impact, six 1A115E uniaxial accelerometers were installed at the locations shown in Fig. 6. Each accelerometer had a range of ±1000 g and a sensitivity of 4.9 mV/g and was bolted in place to reduce the effects of mounting looseness and interface slip on the impact signal. The sensing axis of each sensor was aligned with the impact normal, consistent with the principal drop-motion and hard-impact load directions of the subframe. Therefore, only the local impact-normal acceleration component was measured, while lateral and rotational components were not independently recorded. According to the regional division described above, C1-C2 were located in the main load-bearing cross-beam region, C3 in the central load-transfer cross-beam region, C4-C5 in the wheel-arch beam region, and C6 in the Central circular load-bearing region, as listed in Table 2. The sensor model, range, sensitivity, and mounting method were kept identical across all regions to ensure comparability among the measured responses. Because complete photographs of the test assembly cannot be publicly disclosed owing to confidentiality restrictions associated with the upper mission equipment, the experimental configuration is documented using the schematic in Fig. 6, which shows the sensor layout, acquisition channels, and free-drop procedure.

Table 2 Sensor deployment and related parameters

Region	Structural region	Point(s)	Model	Type	Range (g)	Sensitivity (mV/g)	Axis
I	Main load-bearing cross-beam region	C1—C2	1A115E	1-axis	±1000	4.9	Impact normal
II	Central load-transfer cross-beam region	C3					
III	Wheel-arch beam region	C4—C5					
IV	Central circular load-bearing region	C6					

After installation, the sensors were connected by signal cables to the corresponding channels of a DH5902N dynamic signal acquisition system. A host computer was used to check channel connectivity, zero-point stability, and waveform anomalies in real time. After confirming that the sensors and acquisition channels were functioning normally, a crane lifted the subframe to the specified height, and the actual clearances from the ground were measured at the front-left, front-right, rear-left, and rear-right corners. After the heights and attitude had been recorded and checked, synchronous acquisition was started on all channels. The subframe was then released using a disengagement device, allowed to fall freely, and struck the rigid ground surface. Each channel synchronously recorded the acceleration history during the stationary segment before release, the main-impact segment, and the subsequent vibration-decay segment. The sampling frequency was uniformly set to 50 kHz to ensure complete recording of the primary impact pulse and the mid- and high-frequency structural vibrations.

The nominal drop height was the principal control variable, with conditions of 100, 150, and 200 mm. Apart from drop height, all conditions used the same subframe and additional mass, structural connection state, measurement-point locations, sensor model and mounting method, acquisition equipment, sampling frequency, release method, and contact surface. The subframe mass and the additional mass remained unchanged among the three conditions, so the differences between conditions arose primarily from drop height and the corresponding impact velocity and input energy. One large-scale drop was conducted at each nominal height because repeated testing of the approximately 3.6-t assembly was not feasible under the available project and facility constraints. The results are therefore treated as exploratory. Rotational motion during free fall and impact was not directly measured, and the uniaxial accelerometers recorded only the local impact-normal acceleration component.

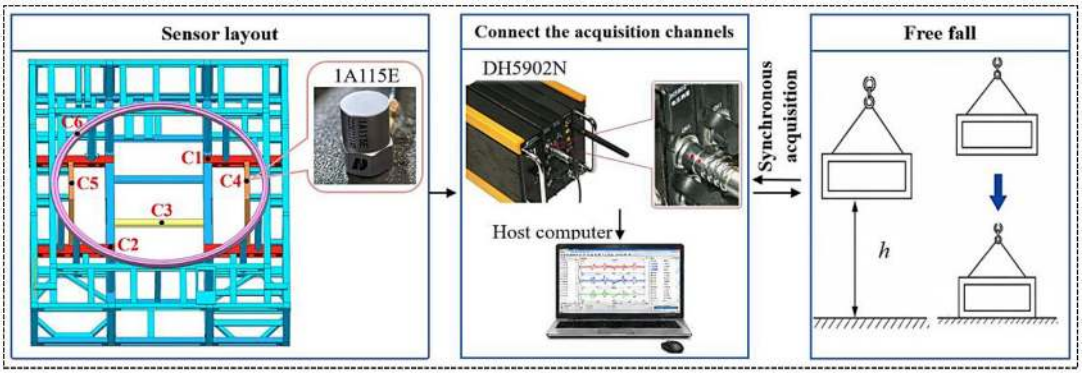


Figure 6 Procedure for the equivalent drop test of the subframe

No initial inclination or horizontal velocity was intentionally imposed, and the subframe was nominally released in an approximately horizontal attitude. However, because the specimen was large and heavy, the four corner points could not be adjusted to exactly the same height owing to the lifting-point locations, differences in sling length, structural mass distribution, and transient disturbance during release. The initial attitude deviation was therefore not treated as an independent test variable, but was recorded as an uncertainty that could not be completely eliminated in a free-drop test of a large-mass specimen. Rotational motion during free fall and impact was not directly measured; therefore, transient pitch and roll histories could not be quantified. The maximum corner-height differences under the three conditions were 11, 8, and 13 mm, respectively; the detailed measurements are listed in Table 3.

Table 3 Initial ground clearances at the four corners under the three drop conditions

Nominal drop height (mm)	Front-left corner (mm)	Front-right corner (mm)	Rear-left corner (mm)	Rear-right corner (mm)	Maximum height difference (mm)
100	93	95	104	95	11
150	148	149	156	150	8
200	195	205	203	208	13

4 DATA PROCESSING AND FEATURE EXTRACTION

4.1 Impact-Signal Preprocessing

Impact-acceleration signals were collected at six measurement points under drop conditions of 100, 150, and 200 mm. For each channel, 20,000 data samples covering the effective impact duration were extracted for analysis. At a sampling frequency of 50 kHz, each time history corresponded to 0.4 s. For each drop condition, the impact onset t_0 was defined as the earliest instant at which the absolute acceleration exceeded 10 g. The same t_0 was applied to all six channels of that condition to preserve the relative timing among measurement points. Before signal preprocessing and feature extraction, the preliminary validity of the raw acceleration data from every channel was checked. The raw-signal peaks are listed in Table 4. All Peak accelerations were within the corresponding sensor ranges, and no clipping caused by insufficient measurement range was observed. In addition, the rising edge, peak segment, and decay segment of the waveform near the principal impact response were continuous, indicating that the acquisition system captured the complete transient acceleration response of the subframe during hard impact.

Table 4 Maximum absolute peaks of the raw data at each measurement point

Point	100 mm (g)	150 mm (g)	200 mm (g)
C1	144	299	378
C2	261	356	379
C3	249	299	322
C4	357	442	785
C5	276	354	819
C6	264	445	722

4.1.1 Wavelet Analysis and Trend Removal

Because of factors such as sensor zero drift, mounting condition, and low-frequency disturbance in the acquisition system, the raw acceleration signal may contain a slowly varying trend. This trend is not a genuine dynamic response generated by the hard impact of the subframe. If it is not removed, it elevates the low-frequency components and affects time-domain integration, RMS calculation, and SRS results (Yao et al., 2020). Wavelet decomposition was therefore used to separate the low-frequency trend from the raw signal. Let the raw acceleration signal at measurement point i be $a_i^b(t)$. Using the sym8 wavelet basis for a $J = 8$-level multiscale decomposition, the signal can be expressed as:

$$a_i^b(t) = A_{i,J}(t) + \sum_{j=1}^{J} D_{i,j}(t) \tag{11}$$

where $A_{i,J}(t)$ is the approximation component at level J, which mainly represents the slowly varying low-frequency trend, and $D_{i,j}(t)$ is the detail component at level j, which mainly contains the primary hard-impact pulse and structural-vibration information. After removing the approximation component, the wavelet-detrended signal is obtained as:

$$a_i^w(t) = a_i^b(t) - A_{i,J}(t) = \sum_{j=1}^{J} D_{i,j}(t) \tag{12}$$

The purpose of this step is to remove baseline drift unrelated to the impact process, thereby preserving the main pulse, secondary responses, and subsequent decaying vibrations more faithfully around the zero baseline rather than attenuating the actual impact components.

To verify the suitability of the wavelet-detrending method, the data from the 100 mm condition were selected and the SRS curves before and after processing were compared, as shown in Fig. 7. After detrending, the anomalous rise in the low-frequency range of the raw signal was suppressed, while the principal spectral shape and response amplitude in the mid- and high-frequency ranges remained essentially unchanged.

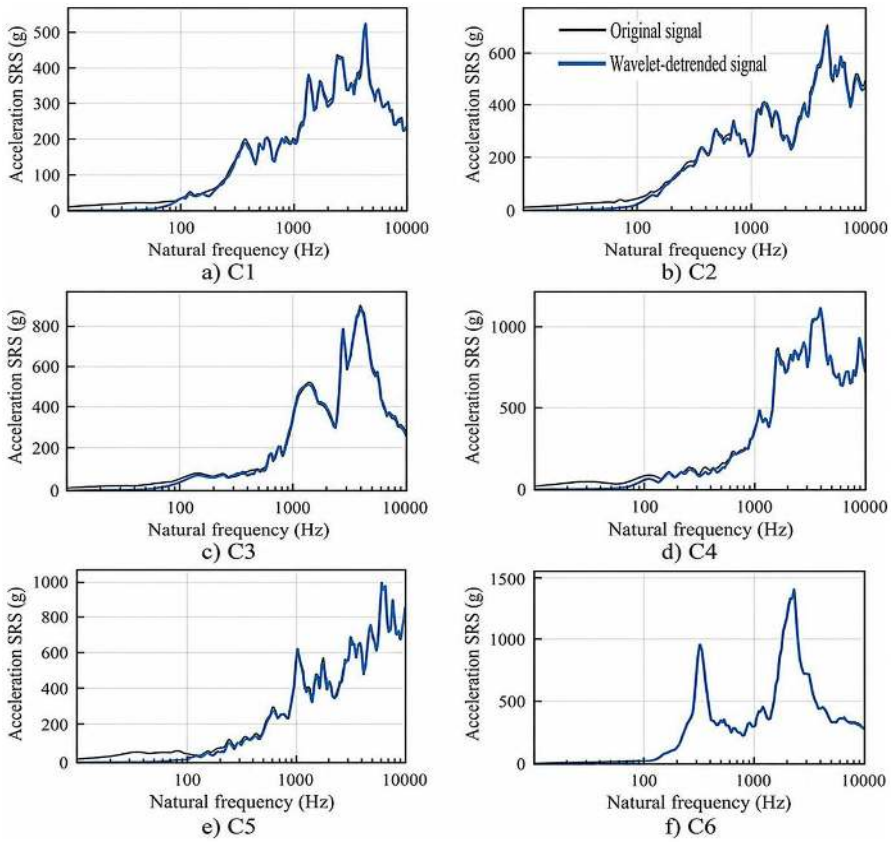


Figure 7 Comparison of SRS results before and after detrending for the 100 mm condition

4.1.2 Low-Pass Filtering and Suppression of High-Frequency Spikes

After trend removal, the signal may still contain high-frequency spikes introduced by the sensor mounting interface, cable disturbance, acquisition circuitry, and environmental noise. Low-pass filtering is therefore required to suppress these components while retaining the effective structural response.

To determine the filter cutoff frequency, the cumulative spectral-energy distribution of the raw signals was first calculated, as shown in Fig. 8. The results indicate that the principal energy at each measurement point was concentrated below 10 kHz, and that the additional energy above 10 kHz was small. A uniform cutoff frequency of 10 kHz was therefore selected for low-pass filtering. The test sampling frequency was 50 kHz, corresponding to a Nyquist frequency of 25 kHz, which is sufficiently higher than the selected cutoff frequency of 10 kHz.

A sixth-order Butterworth prototype was used because of its monotonic and flat passband response. The filter was applied in the forward and reverse directions to obtain zero-phase filtering and avoid a net phase delay in the transient waveform. The processed acceleration signal is expressed as

$$a_i(t) = \mathrm{filtfilt}[H_{\mathrm{LP}}(f_c), a_i^{W}(t)] \tag{13}$$

where $H_{\mathrm{LP}}(f_c)$ denotes a low-pass filter with cutoff frequency $f_c = 10\ \mathrm{kHz}$.

This step suppresses high-frequency spikes and measurement noise that are only weakly related to the dynamic response of the primary structure, while retaining the main hard-impact pulse, secondary collisions, and principal structural-vibration components. Fig. 9 shows the acceleration histories before and after filtering for the 100 mm condition. After filtering, the amplitudes of local high-frequency spikes decreased, whereas the location of the primary impact peak, pulse width, and overall decay trend remained essentially unchanged. For the representative high-response channels, the changes in peak acceleration and RMS caused by low-pass filtering were within 13.7% and 13.0%, respectively, while no measurable shift in the principal peak time was observed. The selected filtering parameters therefore provide an appropriate balance between noise suppression and preservation of the effective response.

After the two processing steps described above, the acceleration histories $a_i(t)$ used in the subsequent analyses were obtained. Wavelet analysis primarily addressed low-frequency baseline drift, while low-pass filtering primarily suppressed high-frequency spikes. Together, these procedures ensured baseline stability at low frequencies and reliability of the transient peaks, providing a consistent data basis for subsequent calculations of Peak acceleration, RMS, and PV-SRS.

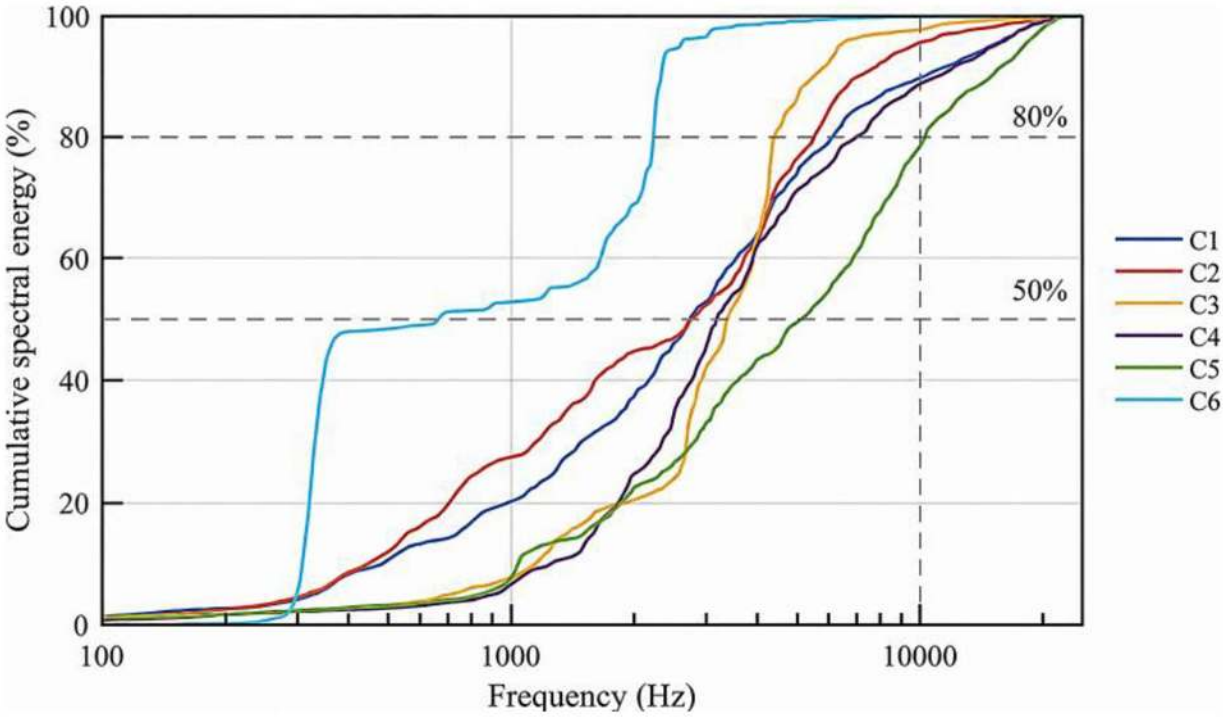


Figure 8 Cumulative spectral-energy distribution of the raw data for the 100 mm condition

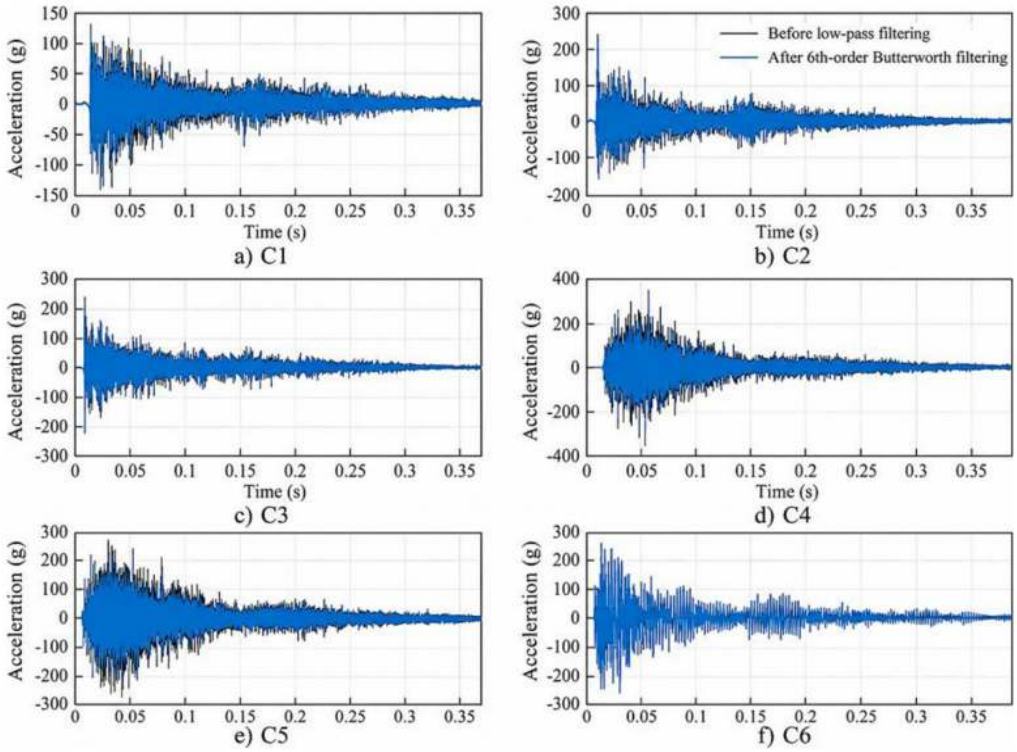


Figure 9 Comparison of time histories before and after filtering for the 100 mm condition

4.2 Time-Domain Metrics and PV-SRS Calculation

Peak acceleration, RMS acceleration, and the PV-SRS were extracted from the preprocessed acceleration signal $a_i(t)$. Each channel contained 20,000 samples at a sampling frequency of 50 kHz, corresponding to a common analysis duration of T = 0.4 s. The Peak acceleration at measurement point i is defined as:

$$a_{p,i} = \max_{0 \le t \le T} | a_i(t) | \tag{14}$$

The root-mean-square value is defined as:

$$a_{\mathrm{RMS},i} = \sqrt{\frac{1}{T}\int_0^T a_i^2(t)\,\mathrm{d}t} \tag{15}$$

The RMS value represents the overall intensity of the acceleration response within the analysis window and can be used to characterize the sustained vibration level.

The PV-SRS characterizes the pseudo-velocity response of equivalent single-degree-of-freedom systems with different natural frequencies to an impact input (Li and Li, 2018). It is calculated using a set of single-degree-of-freedom systems having different natural frequencies and the same damping ratio. For measurement point i, with acceleration $a_i(t)$ used as the base input, the relative-displacement response of a linear single-degree-of-freedom system with natural circular frequency $\omega_n = 2\pi f_n$ and damping ratio ζ satisfies:

$$\ddot{z}_i(t) + 2\zeta\omega_n\dot{z}_i(t) + \omega_n^2 z_i(t) = -a_i(t) \tag{16}$$

where $z_i(t)$ is the displacement of the mass relative to the base, $\omega_n = 2\pi fn$ is the natural circular frequency of the system, and the damping ratio of ζ = 0.05 was adopted as a reference damping level for the PV-SRS calculation rather than as an experimentally identified damping ratio of the present subframe(U.S. Department of Defense, 2022). After Eq. (16) is solved for $z_i(t)$, the relative-displacement shock response spectrum is obtained as:

$$S_{d,i}(f_n) = \max_{0 \le t \le T} | z_i(t; f_n, \zeta) | \tag{17}$$

The PV-SRS is obtained by multiplying the relative-displacement response spectrum by the natural circular frequency:

$$PV_i(f_n) = \omega_n S_{d,i}(f_n) = \omega_n \max_{0 \le t \le T} | z_i(t; f_n, \zeta) | \tag{18}$$

The PV-SRS peak and its Spectrum peak frequency are then extracted as:

$$PV_{p,i} = \max_{f_n \in F} PV_i(f_n) \tag{19}$$

$$f_{PV,i} = \arg\max_{f_n \in F} PV_i(f_n) \tag{20}$$

where F is the frequency range used for the PV-SRS calculation, taken as $f_n \in$ [10, 10000] Hz. $PV_{p,i}$ represents the maximum pseudo-velocity excitation level imposed by the measured impact history on equivalent structural units with different natural frequencies, and $f_{PV,i}$ denotes the frequency at which the spectral response is most pronounced.

Peak acceleration is used herein to characterize local transient impact intensity, RMS to characterize the sustained vibration level, and PV-SRS to analyze frequency-dependent response characteristics in the different regions.

5 RESULTS AND DISCUSSION

To compare hard-impact responses at different subframe locations, Peak acceleration and RMS were used to characterize the local transient extreme and the overall vibration level within the analysis interval, respectively, while PV-SRS was used to evaluate the excitation imposed by the impact history on equivalent structural units with different natural frequencies. This section first discusses changes in the time-domain response at each measurement point with drop height, then analyzes the PV-SRS peaks and their corresponding frequencies, and finally examines impact-load transmission and distribution in relation to the structural region containing each measurement point.

5.1 Time-Domain Response Characteristics

Table 5 lists the peak acceleration and RMS at each measurement point under the three drop conditions, and Figs. 10 and 11 compare the corresponding values among the measurement points.

Table 5 Peak acceleration and RMS at each measurement point under different drop conditions

Condition	Metric	C1	C2	C3	C4	C5	C6
100mm	a_p/g	141	231	226	334	239	261
	a_{RMS}/g	17.1	21.1	22.6	37.6	32.0	37.5
150mm	a_p/g	292	312	304	359	320	446
	a_{RMS}/g	31.7	29.4	30.6	51.2	46.1	57.1
200mm	a_p/g	327	370	325	672	577	707
	a_{RMS}/g	26.6	36.4	34.1	79.0	75.2	86.0

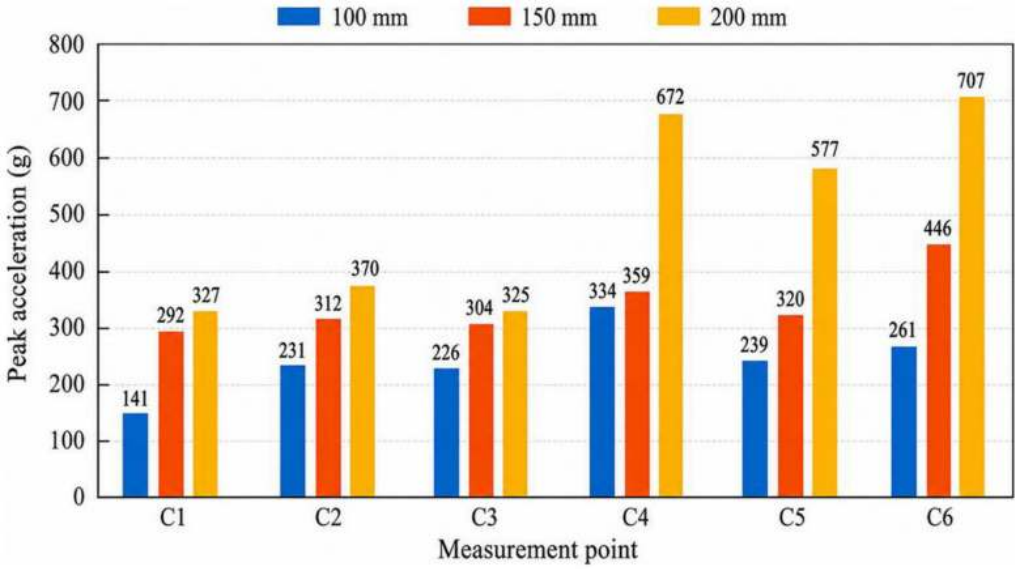


Figure 10 Peak acceleration at each measurement point for different drop heights

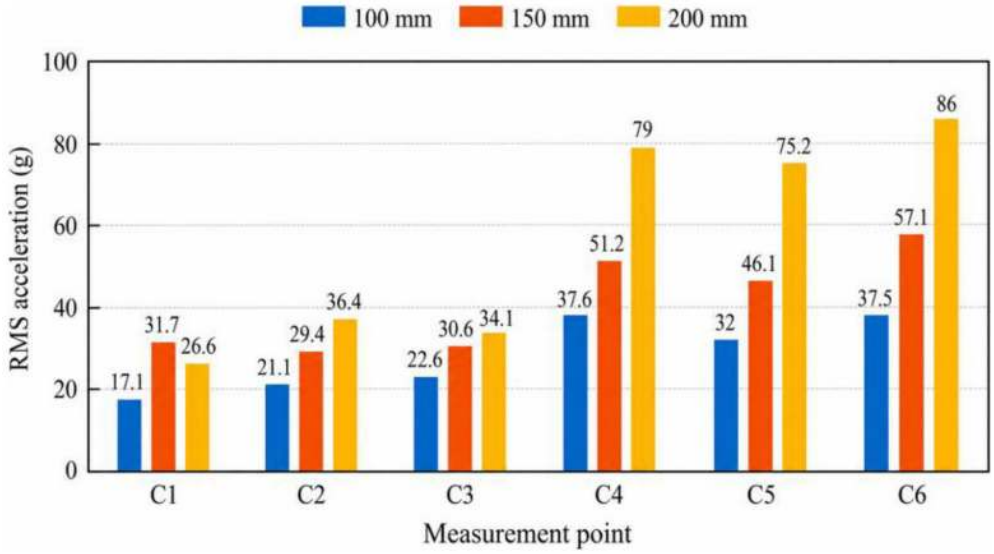


Figure 11 RMS acceleration at each measurement point for different drop heights

As the drop height increased, the peak acceleration and RMS values at most measurement points generally increased, but the magnitude and stage of growth differed among regions. Under the 100 mm condition, the peak at C4 was 334 g, the highest among all measurement points; the RMS values at C4 and C6 were 37.6 and 37.5 g, respectively, and were nearly equal. Under the 150 mm condition, the peak and RMS at C6 increased to 446 g and 57.1 g, making C6 the location with the strongest response under that condition. Under the 200 mm condition, the peaks at C6, C4, and C5 reached 707, 672, and 577 g, respectively, and their RMS values reached 86.0, 79.0, and 75.2 g, all exceeding those at C1-C3. Thus, as the impact input increased, the response became progressively concentrated in the wheel-arch beams region and in the Central circular load-bearing region.

The response increments over different height intervals further reflect changes in the load-transfer paths. Between 100 and 150 mm, the peak values at C1 and C6 increased substantially. Between 150 and 200 mm, the peaks at C4, C5, and C6 increased by 313, 257, and 261 g, respectively, indicating that the dynamic participation of Regions III and IV increased further under the higher input. The peak at C6 under the 200 mm condition was 2.71 times that under the 100 mm condition, and the corresponding ratio for C5 was 2.41, whereas the increase at C3 was comparatively small. These results demonstrate that different structural locations exhibit different response-growth rates as the input increases.

5.2 PV-SRS Peak and Peak-Frequency Characteristics

Table 6 lists the PV-SRS peak and corresponding peak frequency at each measurement point under the three drop-height conditions. Figs. 12 and 13 compare the PV-SRS peaks and their corresponding frequencies, respectively.

The PV-SRS peaks at C6 under the three conditions were 4.60, 6.26, and 6.90 m/s, respectively, all higher than those at the other measurement points. Under the 200 mm condition, the Peak acceleration and RMS values at C4, C5, and C6 were relatively high, whereas their PV-SRS peaks were 1.60, 1.47, and 6.90 m/s, respectively. Thus, impact histories with similar acceleration amplitudes can still differ substantially in their ability to excite equivalent structural units with different natural frequencies.

Table 6 PV-SRS peaks and corresponding frequencies at each measurement point under different drop conditions

Condition	Metric	C1	C2	C3	C4	C5	C6
100mm	$PV_p/(m \cdot s^{-1})$	0.81	1.00	0.80	0.98	0.94	4.60
	f_{PV}/Hz	362	362	133	105	1026	322
150mm	$PV_p/(m \cdot s^{-1})$	1.94	1.80	0.95	1.40	1.18	6.26
	f_{PV}/Hz	439	287	123	211	914	322
200mm	$PV_p/(m \cdot s^{-1})$	1.40	1.70	0.90	1.60	1.47	6.90
	f_{PV}/Hz	532	376	203	246	276	335

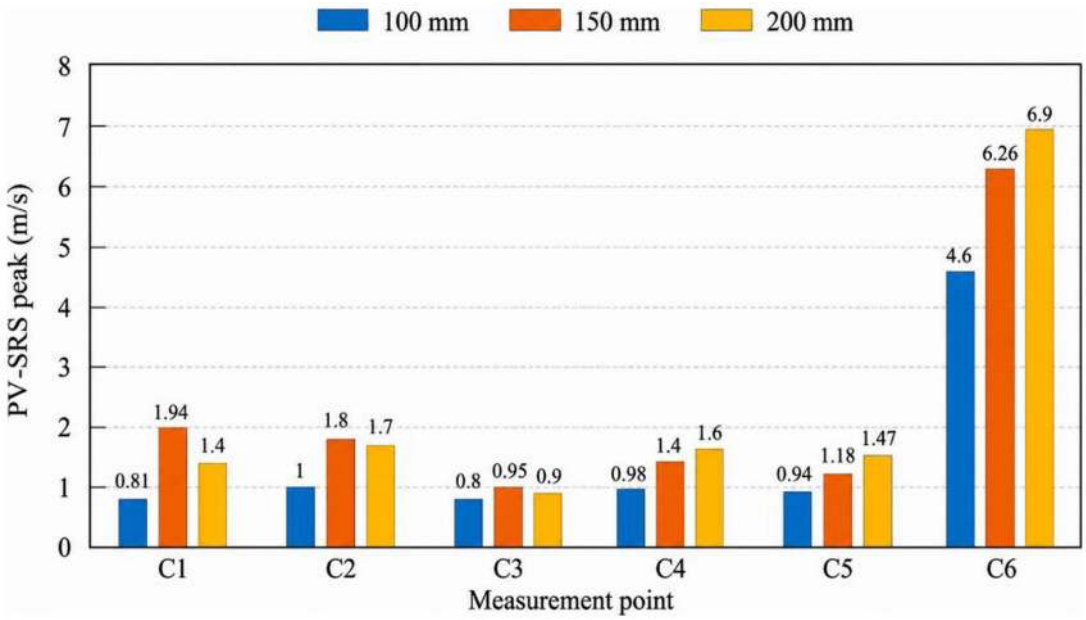


Figure 12 PV-SRS peak at each measurement point for different drop heights

Measurement points with high time-domain responses do not necessarily have comparable PV-SRS levels. For example, under the 200 mm condition, the Peak accelerations at C4 and C6 were 672 and 707 g, and their RMS values were 79.0 and 86.0 g, respectively, so their time-domain metrics were relatively close. Their PV-SRS peaks, however, were 1.60 and 6.90 m/s, respectively, with the value at C6 approximately 4.31 times that at C4. This difference indicates that the C4 response is more characteristic of a high-amplitude broadband impact, whereas the C6 impact history produces a much stronger Pseudo-Velocity Response within a specific frequency band.

Fig. 13 shows that the PV-SRS peak frequencies at the measurement points varied differently with test condition. The peak frequency at C1 increased from 362 Hz to 439 and 532 Hz; that at C2 changed from 362 Hz to 287 and 376 Hz; that at C3 changed from 133 Hz to 123 and 203 Hz; that at C4 increased from 105 Hz to 211 and 246 Hz; and that at C6 remained within 322-335 Hz. With the exception of C5, the peak frequencies at the other measurement points varied within their respective low- to mid-frequency ranges, and the variation at C6 was comparatively narrow.

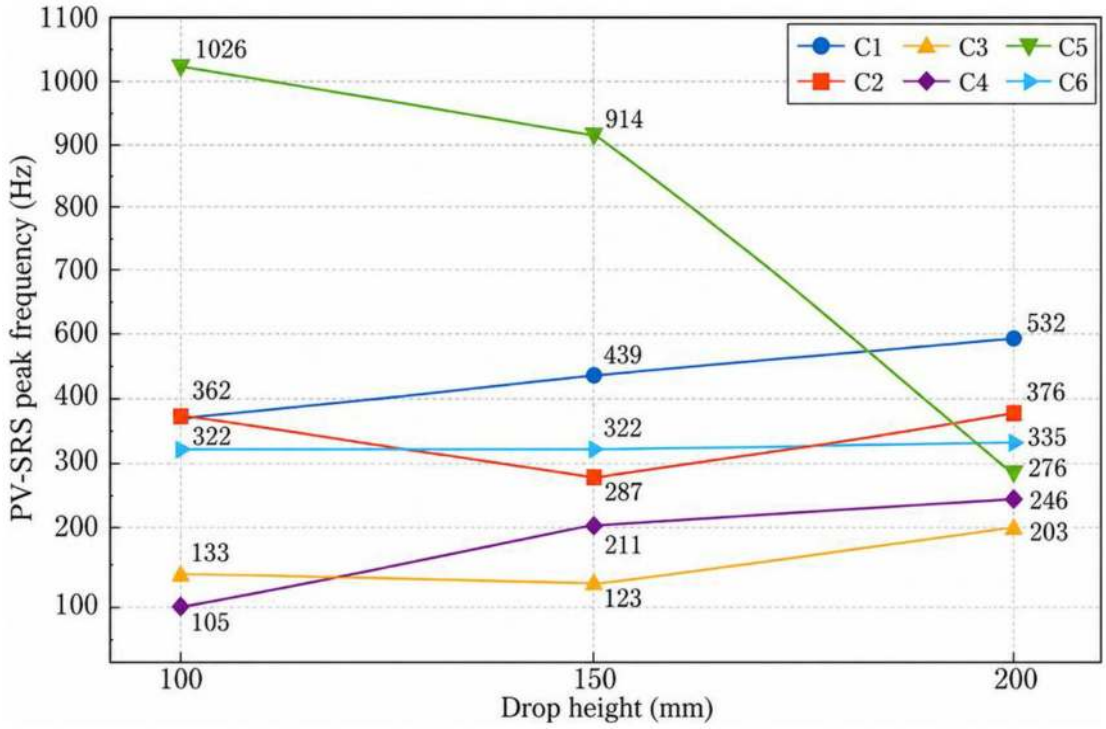


Figure 13 Variation of the PV-SRS peak frequency at each measurement point with drop height

The peak frequency at C5 decreased from 1026 and 914 Hz to 276 Hz, this represents a cross-band shift from the high-frequency range to the low- to mid-frequency range. The resulting trend differed from that observed at C4 in the same region. This phenomenon cannot be interpreted directly as a decrease in structural natural frequency. It is more likely associated with the presence of several spectral peaks of similar amplitude in the C5 PV-SRS. As the impact input increased, the individual peaks grew at different rates, causing the global spectral maximum to switch from the high-frequency peak near 1 kHz to the low- to mid-frequency peak near 276 Hz. The evolution of the complete PV-SRS curve at C5 is examined further in the discussion of Region III in Section 5.3.

These trends are consistent with the regional response model described above. Increasing the drop height changes the impact velocity and contact reaction force $R_c(t)$, while the actual response at each measurement point is also governed by the load-transfer path $T_i[\cdot]$ and by the equivalent mass, stiffness, and damping of the region. Responses at the measurement points therefore do not increase in proportion to the drop height or input energy, and some indices exhibit non-monotonic variations. The complete PV-SRS curves and the evolution of their spectral shapes in the individual structural regions are analyzed in Section 5.3.

5.3 Region-Specific Response Characteristics

The four structural regions are discussed separately below by combining the peak acceleration, RMS acceleration, and complete PV-SRS curves.

Region I: Main load-bearing cross-beam region

Region I contains C1 and C2 and primarily reflects impact transmission at the connections between the main load-bearing cross-beams and longitudinal beams. Under all three conditions, the Peak acceleration at C2 exceeded that at C1, but the difference decreased from 90 g under the 100 mm condition to 20 g under the 150 mm condition and then increased to 43 g under the 200 mm condition. This indicates that load distribution within the connection region changed with the test condition.

The Peak acceleration at C1 increased with drop height, whereas its RMS reached 31.7 g under the 150 mm condition and then decreased to 26.6 g. At C2, both Peak acceleration and RMS increased with height. Under the 150 mm condition, the Peak acceleration at C1 was lower than that at C2, but its RMS and PV-SRS peak were 31.7 g and 1.94 m/s, respectively, slightly higher than the corresponding values of 29.4 g and 1.8 m/s at C2. This indicates that the C1 response under this condition was not governed by a single transient extreme; impact duration and frequency composition also influenced its RMS and PV-SRS.

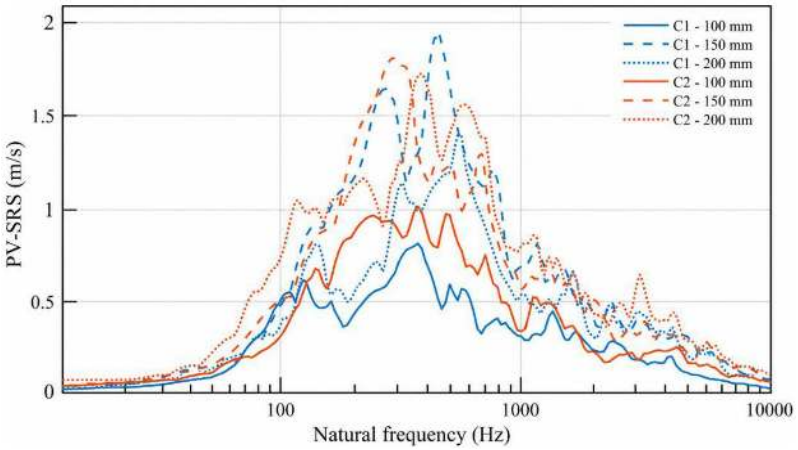


Figure 14 PV-SRS curves of the Region I for different drop heights

Fig. 14 shows that the Region I PV-SRS is distributed mainly in the mid-frequency range and contains several adjacent spectral peaks. Under the 100 mm condition, the peak frequencies at C1 and C2 were both 362 Hz. As the input increased, the peak frequencies at the two points gradually separated. This difference may be related to variations in local configuration and boundary conditions at the cross-beam-to-longitudinal-beam connections. Considering all three indices, Region I primarily exhibits impact transmission and condition-dependent load redistribution within the main load-bearing beam system. Although its response level is lower than those of Regions III and IV, location-dependent differences within the region still warrant attention.

Region II: Central load-transfer cross-beam region

Only measurement point C3 was located in Region II. Its Peak acceleration increased from 226 g to 304 and 325 g, while its RMS increased from 22.6 g to 30.6 and 34.1 g, showing a relatively gradual increase with drop height. From 100 to 200 mm, the Peak acceleration and RMS at C3 increased to 1.44 and 1.51 times their initial values, respectively, both smaller than the corresponding increases in Regions III and IV.

The PV-SRS peak at C3 ranged from 0.80 to 0.95 m/s and changed little among the three conditions. The spectra in Fig. 15 exhibit multiple peaks of similar amplitude, with no single frequency band remaining continuously dominant. The peak frequency changed from 133 Hz to 123 and 203 Hz, indicating that the relative contribution of the low- to mid-frequency response increased under the high-input condition, although the PV-SRS peak did not increase substantially at the same time.

C3 can therefore serve as a reference location for regional response comparisons under the present conditions. It should be emphasized that lower acceleration and PV-SRS values do not directly imply a larger strength margin in this region. The central load-transfer cross-beam still transfers loads between adjacent beam systems, and its engineering design should focus on maintaining continuity of the load-transfer path.

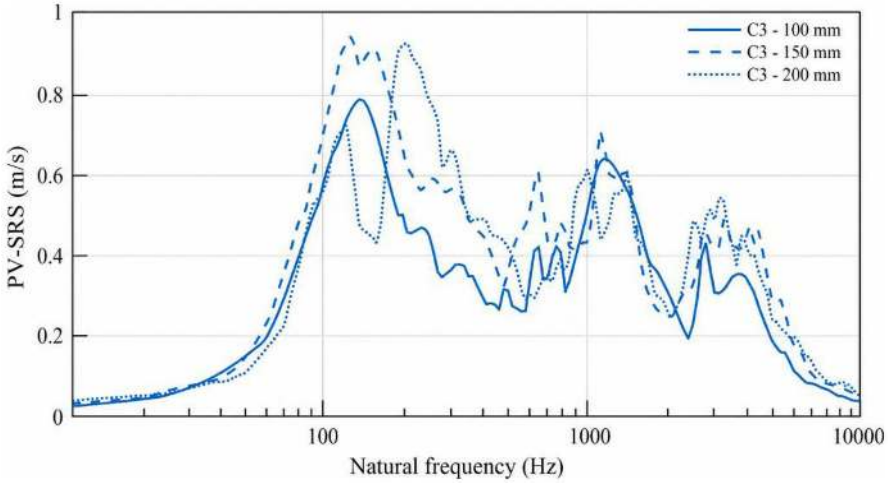


Figure 15 PV-SRS curves of the Region II for different drop heights

Region III: Wheel-arch beam region

Region III contains C4 and C5, and both measurement points exhibit pronounced stage-dependent behavior. Between 100 and 150 mm, the Peak accelerations at C4 and C5 increased by 7.5% and 33.9%, respectively. Between 150 and 200 mm, the corresponding increases were 87.2% and 80.3%, while the RMS values increased by 54.3% and 63.1%, respectively. Thus, when the drop height reached 200 mm, the time-domain responses of the wheel-arch beams began to increase much more rapidly.

The Peak acceleration at C4 was higher than that at C5 under all three conditions, but the difference narrowed as the input increased. The C4-to-C5 peak acceleration ratio decreased from 1.4 under the 100 mm condition to 1.16 under the 200 mm condition, and the RMS ratio decreased from 1.18 to 1.05. Under the high-input condition, the C5 response therefore approached that at C4, and the response distribution within Region III changed from relative concentration at C4 to similarly high levels at both measurement points.

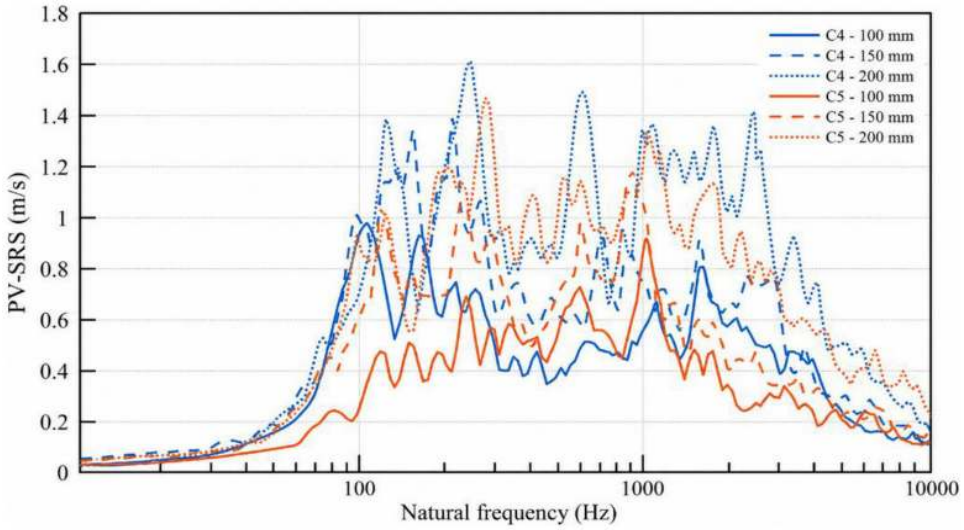


Figure 16 PV-SRS curves of the Region III for different drop heights

Fig. 16 shows that the PV-SRS curves at C4 and C5 both have multi-peak, broadband distributions, although their spectral peaks evolve differently.

The PV-SRS peak at C4 increased from 0.98 m/s to 1.40 and 1.60 m/s, while the corresponding frequency increased progressively from 105 Hz to 211 and 246 Hz; the response peak therefore remained in the low- to mid-frequency range. The PV-SRS peak at C5 increased from 0.94 m/s to 1.18 and 1.47 m/s, whereas the corresponding frequency decreased from 1026 and 914 Hz to 276 Hz.

The spectral evolution shows that, under the 100 and 150 mm conditions, C5 had both low- to mid-frequency and high-frequency response peaks. The peak near 1 kHz was higher and was therefore identified as the global spectral peak. When the drop height increased to 200 mm, the low- to mid-frequency peak grew more than the original high-frequency peak, shifting the global maximum to 276 Hz. The decrease in C5 peak frequency therefore primarily represents spectral-peak switching caused by changes in the relative amplitudes of multiple peaks and cannot be interpreted directly as a reduction in structural natural frequency.

At the same time, the difference between the C4 and C5 peak frequencies decreased from 921 Hz under the 100 mm condition to 30 Hz under the 200 mm condition, suggesting that the relative contributions of the low- to mid-frequency responses at the two points became similar under the high-input condition. Although the two points belong to the same region, differences in local geometric transitions, connection locations, and load-transfer paths can still produce different frequency-band responses at low input levels.

Region IV: Central circular load-bearing region

C6 was one of the measurement points with the highest overall response under all three conditions. Its Peak acceleration increased from 261 g to 446 and 707 g, and its RMS increased from 37.5 g to 57.1 and 86 g, indicating that the Central circular load-bearing region is highly sensitive to input intensity.

The PV-SRS peaks at C6 were 4.60, 6.26, and 6.90 m/s, approximately 4.6, 3.2, and 4.1 times the second-highest value under the respective conditions. Even under the 100 mm condition, when the C6 acceleration peak was not the highest among all measurement points, its PV-SRS still exceeded those at all other points. This indicates that the region responds strongly to input within a specific frequency band.

Figure 17 shows that the principal spectral peak at C6 remained within 322-335 Hz. As the drop height increased, the peak amplitude rose continuously, while the peak frequency changed by less than 4%. This behavior may be related to the convergence of multiple load-transfer paths and the local dynamic characteristics of the Central circular load-bearing region.

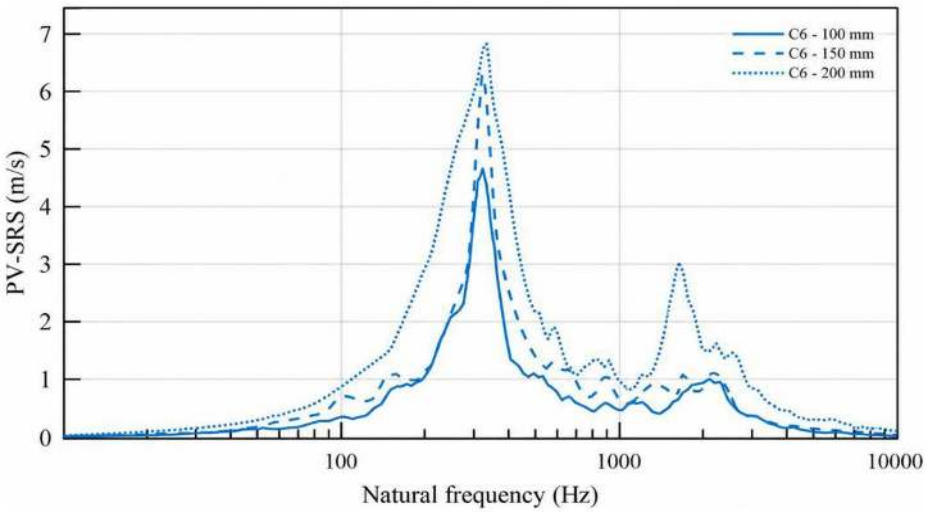


Figure 17 PV-SRS curves of the Region IV for different drop heights

Under the 200 mm condition, a secondary spectral peak also appeared in the 1-2 kHz range, indicating increased participation of local higher-order responses at high input. Under the same condition, the Peak acceleration and RMS at C6 were relatively close to those at C4, but its PV-SRS was approximately 4.3 times that at C4. Two types of high-response region can therefore be distinguished: C4 is more representative of a broadband, high-amplitude impact, whereas C6 exhibits response concentration within a specific frequency band.

5.4 Discussion

Considering the peak, RMS, and PV-SRS results together, the four regions can be summarized as exhibiting distinct response modes. Region I is characterized mainly by load transmission through connections and load redistribution. The response in Region II changes relatively gradually with drop height under the present conditions and exhibits transitional load-transfer behavior. Region III shows enhanced broadband response under high-input conditions. Region IV exhibits a high overall response with a comparatively concentrated dominant frequency band.

These differences show that subframe hard impact is not governed by a single amplitude measure. Peak acceleration primarily identifies local transient extremes, RMS reflects the overall vibration level following impact, and PV-SRS distinguishes sensitivity in different frequency bands. Regions III and IV both exhibit high time-domain metrics, but their spectral characteristics differ; their structural optimization objectives should therefore also differ.

From an engineering perspective, the Central circular load-bearing region should be treated as a priority location for verification. Particular attention should be paid to the dominant 300-350 Hz band, the secondary 1-2 kHz band, and the connections between the annular members and the cross-beams, diagonal braces, and supports. For the wheel-arch beams region, cross-sectional changes, geometric transitions, and load-diffusion paths should be improved to avoid abrupt stiffness transitions. The main load-bearing beam connection region should maintain consistency in cross-beam-to-longitudinal-beam connections, welds, and assembly conditions, while the central load-transfer cross-beam should maintain continuity of the load-transfer path.

Several limitations should be noted. Only one large-scale drop was conducted at each nominal height, and rotational motion during free fall and impact was not directly measured. In addition, the uniaxial accelerometers measured only the local impact-normal component. The static FE analysis is therefore used only as a qualitative aid for interpreting load-transfer characteristics rather than as a dynamically validated simulation of the complete impact process.

6 CONCLUSIONS

This study addressed the hard impact that an airdrop subframe may experience during the late stage of airbag cushioning. Based on structural function, load-transfer paths, local configuration, and stiffness-transition characteristics, the six measurement points were assigned to four analysis regions. Equivalent drop tests were conducted from heights of 100, 150, and 200 mm, and Peak acceleration, RMS, and PV-SRS were used to evaluate the four structural regions represented by the six measurement points. The principal conclusions are as follows.

1. Based on the principle of residual-velocity equivalence, the hard-contact process during the late cushioning stage of airdrop equipment was converted into a free-drop impact problem of the subframe. An analysis model comprising contact compression, nonlinear contact reaction force, load transmission, and regional dynamic response was established. The response at a measurement point depends not only on impact velocity and contact input, but also on the structural load-transfer path and the mass, stiffness, and damping characteristics of the region. On this basis, the upper laboratory input level was estimated using the reported mean landing-impact acceleration limit of 20 g together with an assumed equivalent duration of 10 ms, giving a nominal upper drop height of approximately 200 mm. The 100 and 150 mm conditions provided graded lower input levels. The 10 ms duration is an engineering approximation rather than a measured duration of the present hard-contact event. The subframe was divided into four regions according to structural function, load-transfer paths, and local configuration, forming a test-evaluation method comprising three drop conditions, four structural regions, and six measurement points.
2. As drop height increased, the Peak acceleration and RMS at most measurement points generally increased, but the stage and magnitude of growth differed among points. Under the 200 mm condition, the Peak accelerations at C6, C4, and C5 reached 707, 672, and 577 g, respectively, and their RMS values reached 86, 79, and 75.2 g. The high time-domain responses were concentrated mainly in the wheel-arch beams region and in the Central circular load-bearing region. PV-SRS emphasizes aspects of the response different from those emphasized by the time-domain metrics. The PV-SRS peaks at C6 under the three conditions were 4.6, 6.26, and 6.9 m/s, and the peak frequency remained within 322-335 Hz. The peak frequency at C5 decreased from 1026 and 914 Hz to 276 Hz, primarily reflecting a switch in the dominant spectral peak caused by changes in the relative amplitudes of multiple peaks; it cannot be interpreted directly as a reduction in structural natural frequency. Peak acceleration, RMS, and PV-SRS characterize the transient extreme, overall vibration level, and frequency-dependent response, respectively, and are mutually complementary.
3. The four structural regions exhibited different hard-impact response characteristics. Region I primarily reflected impact transmission and condition-dependent load redistribution at the connections between the main load-bearing cross-beams and longitudinal beams. The indices in Region II varied comparatively gradually with drop height, and this region mainly provided transitional load transfer between adjacent beam systems. In Region III, the increases in Peak acceleration and RMS were relatively large between 150 and 200 mm; the time-domain responses at C4 and C5 became progressively closer, while the dominant peak at C5 shifted from the high-frequency range to the low- to mid-frequency range, indicating an increase in the relative contribution of low- to mid-frequency beam-system response. In Region IV, C6 exhibited a high overall response and a comparatively concentrated dominant frequency band. The results demonstrate the spatial nonuniformity of the subframe hard-impact response. Combining structural region division with multi-index evaluation can distinguish transient intensity, vibration persistence, and frequency-dependent response among different load-bearing regions.

The present findings are limited to the investigated subframe configuration, the approximately 3.6-t test assembly, rigid-ground vertical impacts, nominally horizontal release, the three nominal drop heights of 100, 150, and 200 mm, and the six investigated measurement locations. Because only one large-scale drop was conducted at each height, the observed differences should be regarded as exploratory and should not be interpreted as statistically generalizable trends.

ACKNOWLEDGEMENTS

The authors thank Guizhou Aerospace Tianma Electromechanical Technology Co., Ltd. for providing experimental resources and technical support.

This research is supported by the Research on Key Technologies and Equipment for Intelligent Rapid Excavation in Coal Mines under Complex Conditions in Southwest China (Grant No. QJJ [2025]003). Research on Key Technologies of Automatic Transmission Health Management Based on Deep Learning (Grant No. Qian Ke He supported [2026] General 182).

Author's Contributions: Y. Shi: investigation, formal analysis, writing. S. Yuan: supervision, writing—review and editing. P. Wu, B. Hu, and L. Fu: methodology and technical guidance. J. X. Luo: investigation and data processing. Z. W. Yang: resources and technical support.

Data availability statement: The datasets generated and analyzed during the current study are available from the corresponding author upon reasonable request.

Editor: Marcilio Alves.

References

ACADEMY OF ARMORED FORCE ENGINEERING, PLA. (2017). Simulation and evaluation method for airdrop landing under complex environmental conditions: CN104166771B. (in Chinese).

FU X H, WANG J, CHEN Y, et al. (2021). Simulation model of the landing cushioning process for manned airdrop of combat vehicles. Journal of Vibration and Shock 40(24): 57–64. (in Chinese).

He H, Chen Z, He C, et al. (2015). A hierarchical updating method for finite element model of airbag buffer system under landing impact. Chinese Journal of Aeronautics 28(6): 1629–1639.

HONG H J, WANG H Y, LI J Y, et al. (2015). Evaluation method for the airbag cushioning system of airdrop equipment. Journal of Mechanical Engineering 51(4): 148–154.

Hou D, Li Q M. (2023). Damage boundaries on shock response spectrum based on an elastic single-degree-of-freedom structural model. International Journal of Impact Engineering 173: 104435.

Hou J, Yu G, Zhang W, et al. (2019). Test research on airdrop shock vibration of armored vehicles. IOP Conference Series: Materials Science and Engineering 616(1): 012033.

Li B W, Li Q M. (2018). Damage boundary of structural components under shock environment. International Journal of Impact Engineering 118: 67–77.

LI J Y, LI L W, LIU C S, et al. (2022). Simulation of cushioning characteristics of interconnected airbags for heavy equipment airdrop. Packaging Engineering 43(1): 278–284. (in Chinese).

Li Z, Yu Z, Li X, et al. (2025). Active Rollover Prevention Mechanism and Landing Attitude Control for Vehicle Airdrop. Aerospace 12(10): 905.

LIAN W, HOU B, SUN J, et al. (2022). Numerical analyses of heavy equipment airdrop with cushion airbag landing process impacting the rigid and soil ground. Advances in Aeronautical Science and Engineering 13(1): 68–75.

Lu C, Chen J, Wang C, et al. (2024). Landing cushioning analysis of new generation heavy airborne armored vehicles. Aircraft Engineering and Aerospace Technology 96(4): 621–630.

LU C Y, CHEN J B, WANG C, et al. (2023). Cushioning performance of combined airbags for heavy equipment airdrop. Journal of Astronautics 44(6): 841–850. (in Chinese).

Timmers R, Hardy R, Welch J. (2009). Modeling and simulation of the second-generation Orion Crew Module airbag landing system. 20th AIAA Aerodynamic Decelerator Systems Technology Conference and Seminar: 2921.

U.S. Department of Defense. (2022). MIL-STD-810H with Change 1: Environmental Engineering Considerations and Laboratory Tests, Method 516.8—Shock. Washington, DC, USA.

Wang Y, Wang G, Sun Y, et al. (2025). Airdrop dynamics modeling and simulation based on reduced multibody system transfer matrix method. Aerospace Science and Technology 158: 109914.

Wang Y, Yang C. (2023). Modeling and Application of Out-of-Cabin and Extra-Vehicular Dynamics of Airdrop System Based on Kane Equation. Aerospace 10(10): 905.

Xinyi S, Xuefeng W, Caishan LI U. (2025). A review of the airbag landing system for spacecraft. Chinese Journal of Aeronautics 38(8): 103569.

Xu Y, Tian Y, Li Q, et al. (2022). Vibro-impact response analysis of collision with clearance: A tutorial. Machines 10(9): 814.

Yan Y, Li Q M. (2019). Low-pass-filter-based shock response spectrum and the evaluation method of transmissibility between equipment and sensitive components interfaces. Mechanical Systems and Signal Processing 117: 97–115.

Yan Y, Li Q M. (2021). Design and implementation of net zero displacement filter for the synthesis of a mechanical shock signal under specified shock response spectrum. Mechanical Systems and Signal Processing 147: 107105.

YANG Z H, LIU C S, LI J, et al. (2022). Dynamic modeling and simulation of the landing cushioning process of airborne vehicles. Acta Armamentarii 43(S1): 26–34. (in Chinese).

Yao X, Zhang W, Wang Z, et al. (2020). Acceleration signal processing method of impact response of floating shock platform based on rigid body motion model. Shock and Vibration 2020(1): 8826675.

Yuan C, Xian long J. (2010). Dynamic response of flexible container during the impact with the ground. International Journal of Impact Engineering 37(10): 999–1007.

Zhang C, Zhao Y, Shen Y, et al. (2024). The modeling and analysis of vibration response with airdrop vehicle in landing process. Journal of the Brazilian Society of Mechanical Sciences and Engineering 46(6): 345.

Zhang Z, Zhang H, Chen Y, et al. (2023). Research on dynamic load estimation method of crawler travel system. Journal of Mechanical Science and Technology 37(2): 555–567.

Zhao Q, Wang H, Lu C, et al. (2025). Design and Analysis of a Cushioning Airbag System for Heavy Airdropped Equipment in High-Altitude Environments. Aerospace 12(9): 768.

Zhou X, Zhou S, Li D, et al. (2022). Research on design and cushioning performance of combined lunar landing airbag. Acta Astronautica 191: 55–78.